Theoretical models to predict the flexural failure of reinforced concrete beams under blast loads

Carta G. [a] and Stochino F. [b]

[a] Corresponding author

Affiliation: Department of Mechanical, Chemical and Materials Engineering, University of Cagliari

Address: Via Marengo 2, 09123 Cagliari, Italy

Telephone number: +39 070 675 5410

Fax number: +39 070 675 5418

E-mail address: giorgio_carta@unica.it

[b] Affiliation: Department of Civil and Environmental Engineering and Architecture, University of Cagliari

Address: Via Marengo 2, 09123 Cagliari, Italy

Telephone number: +39 070 675 5410

Fax number: +39 070 675 5418

E-mail address: fstochino@unica.it

Abstract

This paper presents two alternative approaches for the study of reinforced concrete beams under blast loads. In the first approach, the beam is modeled by means of Euler-Bernoulli's theory and its elastic-plastic behavior is expressed through a new nonlinear relationship between bending moment and curvature. In the second approach, instead, the beam is idealized as a single degree of freedom system. The effects of strain rate, which are of paramount relevance in blast problems, are taken into consideration by introducing time-variable coefficients into the equations of motion derived from the two models. The latter are employed to assess the time-history of the maximum deflection of a simply supported beam subjected to a uniformly distributed blast load. By comparing the theoretical results with some experimental findings available in literature and with the solution obtained from a commercial finite element software, it is found that the first approach is capable of

accurately evaluating the maximum deflection of the beam at failure; on the other hand, the second approach provides a less precise prediction, however it is simpler to implement in practice because it requires less computational effort.

Keywords: Reinforced concrete beams; blast loads; continuous beam model; SDOF model; strain rate; deflection time-history.

1. Introduction

The effects of explosions on structures can be tremendously dangerous, since they can cause severe damage to buildings and, consequently, loss of lives. Explosions can be ascribed to military events or civilian accidents, like detonations of bombs or other weapons, reactions of certain chemicals, bursts of gas cylinders, and so on. Since the loads due to blast overpressure can be very intense, structural elements should be endowed with enough strength and, above all, ductility to resist such loads. In this paper, the attention is focused on under-reinforced concrete beams, which generally exhibit flexural failure.

Experimental results of structural elements subjected to blast loads are hardly found in literature. This is due not only to national security reasons (the spread of knowledge on this topic is often limited by Countries for defense purposes), but also to the fact that experiments of this kind are costly and difficult to carry out. Fortunately, there are some remarkable exceptions. For instance, Hudson and Darwin [1] damaged several reinforced concrete beams using explosives and, after strengthening some of them with carbon fiber reinforced polymers, examined if the repaired beams exhibited enhanced flexural capacity with respect to the unrepaired ones. Magnusson and Hallgren [2-5] subjected many reinforced concrete beams made of normal or high strength concrete, with or without steel fibers, to air blast loading; they discovered that the beams with a high reinforcement ratio and without steel fibers failed in shear, while those with a low reinforcement ratio failed in flexure. It is important to mention also the experimental works by Remennikov and Kaewunruen [6], Fujikake et al. [7] and Tachibana et al. [8], in which reinforced concrete beams under impact loads were investigated, and the contributions by Alves and Jones [9], Lawver et al. [10] and Nassr

et al. [11], who analyzed the behavior of steel members under impact or blast loads; though quite interesting, the results of these studies are not considered in the present paper, since they are not relevant to the scope of this work.

The determination of the dynamic response of a reinforced concrete beam under blast loads is not an easy task, partly because of the complexity in modeling the structural element (considering that the behavior of the beam under such loads is generally nonlinear and that the properties of the materials are functions of the strain rate) and partly because of the difficulty in defining precisely the time variation and the space distribution of the load. Therefore, different simplified methods have been proposed so far. The most elementary and common approach consists in schematizing the beam with a single degree of freedom (SDOF) system [12-15,11]; this approach simplifies both the theoretical formulation of the problem and the calculations, but it usually requires the introduction of empirical formulae and, in addition, it does not provide full information on the beam response. More advanced methods are based on multi-degree of freedom (MDOF) discretization, whereby the beam is divided into finite elements along its length; in the most sophisticated formulations, each element is also subdivided into fibers along its depth, in order to take into account the variation of strain rate over the cross-section [7,16].

In this paper, a continuous model for the reinforced concrete beam (that is referred to as "continuous beam model" in the following) is proposed, in which the inelastic behavior of the beam is represented by a smooth relationship between bending moment and curvature and in which the effects of strain rate are taken into account, as described in Section 2. Furthermore, an idealization of the beam through an equivalent SDOF system is presented in Section 3, where again strain rate effects are considered. The continuous beam model and the SDOF model are employed in Section 4 to derive the time-history of the maximum deflection of a simply supported reinforced concrete beam under blast loads; the validity of these two theoretical approaches is checked by comparing the results they produce with experimental data available in literature and with the solution given by a commercial finite element code. Finally, some concluding remarks are provided in Section 5.

2. Continuous beam model

2.1 Equation of motion of beams under distributed loads

In order to model a reinforced concrete (RC) beam before collapse, Euler-Bernoulli's theory is adopted, which assumes that plane sections remain plane and perpendicular to the beam axis after deformation. An infinitesimal segment of the beam in its deformed configuration is represented in Fig. 1, where v denotes transverse displacements, M is the bending moment, V is the shear force and q is the transverse distributed load. All these quantities are generally functions of both the undeformed axis coordinate x and time t.
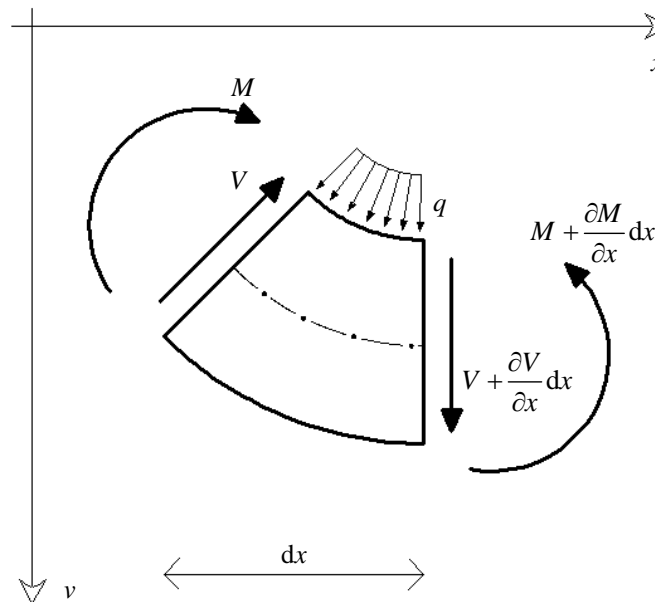

Fig. 1: Internal and external forces acting on an infinitesimal element of the beam.

Equilibrium conditions require that [17,§ 3.1.1]

$$\frac{\partial^2 M}{\partial x^2} + q = \mu \frac{\partial^2 v}{\partial t^2},$$

(1)

where μ stands for the mass per unit length of the beam. Eq. (1) should be satisfied for any constitutive properties of the beam.

The next step is to specify the nonlinear material behavior of the RC beam. In practical applications,

for an under-reinforced concrete beam a bilinear relationship[*] between bending moment and

curvature is commonly assumed. Though quite convenient from a computational point of view, this

relationship hardly mimics the real behavior of the beam, which rarely exhibits a sharp transition

between the elastic and the plastic deformation regimes. Therefore, in this work a smoother

relationship between the bending moment M and the curvature θ is introduced, which reads

$$M = \bar{M} \tanh\left(\frac{\bar{K}}{\bar{M}}\theta\right) = -\bar{M}\tanh\left(\frac{\bar{K}}{\bar{M}}\frac{\partial^2 v}{\partial x^2}\right). \tag{2}$$

The hyperbolic tangent function is used in Eq. (2) because it does not present any slope

discontinuity and is capable of fitting well a bilinear function by a proper choice of its coefficients.

The parameter $\bar{M}$ and $\bar{K}$ appearing in Eq. (2), which represent the equivalent ultimate bending

moment and the initial flexural rigidity of the beam respectively, depend on the sectional and

constitutive properties of the beam (as illustrated in more detail in Subsection 2.2). The minus sign

in front of the right-hand side term takes into account that a positive bending moment (which,

conventionally, causes compression in the top fibers and tension in the bottom ones) produces a

negative curvature in the reference system chosen in Fig. 1. It should be observed that the right-

hand side term of Eq. (2) is obtained by assuming small deformations and rotations in the beam.

The introduction of a unique relation between bending moment and curvature also allows to use a

single equation of motion, without the need to split Eq. (1) into one equation for the elastic range

and another one for the elastic-plastic range, as instead required if a bilinear relationship is

considered. Moreover, unloading can be ignored in dynamic problems concerning explosions, since

the maximum response of the beam to blast loads is usually found before unloading occurs [18].[†]

By substituting Eq. (2) into Eq. (1), the following differential equation of motion in the only

unknown v is derived:

---

[*] A more sophisticated approach would be to adopt a trilinear relationship between bending moment and curvature, which would take into account also the initial state before concrete cracking occurs. Here this initial state is not considered, since the tensile strength of concrete will be neglected, as stated in Subsection 2.2.
[†] This is the reason why damping has been neglected from the formulation.

$$\bar{K}\,\text{sech}^2\left(\frac{\bar{K}}{\bar{M}}\frac{\partial^2 v(x,t)}{\partial x^2}\right)\left[-2\frac{\bar{K}}{\bar{M}}\tanh\left(\frac{\bar{K}}{\bar{M}}\frac{\partial^2 v(x,t)}{\partial x^2}\right)\left(\frac{\partial^3 v(x,t)}{\partial x^3}\right)^2 + \frac{\partial^4 v(x,t)}{\partial x^4}\right] + \mu\frac{\partial^2 v(x,t)}{\partial t^2} = q(x,t). \quad (3)$$

2.2 Neutral axis depth and bending moment at the yield and ultimate states

The parameters $\bar{M}$ and $\bar{K}$ appearing in Eqs. (2) and (3) can be determined from the values of the neutral axis depth and of the bending moment at the yield and ultimate states, as it will be explained in the following.

First of all, the constitutive properties of the materials of which the RC beam is made should be specified. They are extracted from the *fib Bulletin n. 55* [19]. In particular, the uniaxial stress-strain relation of concrete is given by [19,§ 5.1.8.1]

$$\sigma_c = f_{cm}\frac{k\cdot\varepsilon_c/\varepsilon_{c1} - (\varepsilon_c/\varepsilon_{c1})^2}{1+(k-2)\cdot\varepsilon_c/\varepsilon_{c1}} \quad \text{for } |\varepsilon_c| < |\varepsilon_{c,\text{lim}}|, \quad (4)$$

where σ_c (<0) and ε_c (<0) are concrete compressive stress and strain, respectively, while f_{cm}, ε_{c1}, $\varepsilon_{c,\text{lim}}$ and k are quantities that depend on the concrete grade [19,Table 5.1-8]. The compressive stress-strain diagram of concrete for a generic concrete grade is shown in Fig. 2a. It should be pointed out that the tensile strength of concrete is neglected.

The uniaxial behavior of reinforcing steel - both in tension and in compression - is approximated by an elastic - perfectly plastic diagram, as shown in Fig. 2b [19,§ 5.2.9]. In this figure, E_s denotes the Young's modulus of steel, f_{yk} indicates its yield strength and ε_{sy} stands for its yield strain.
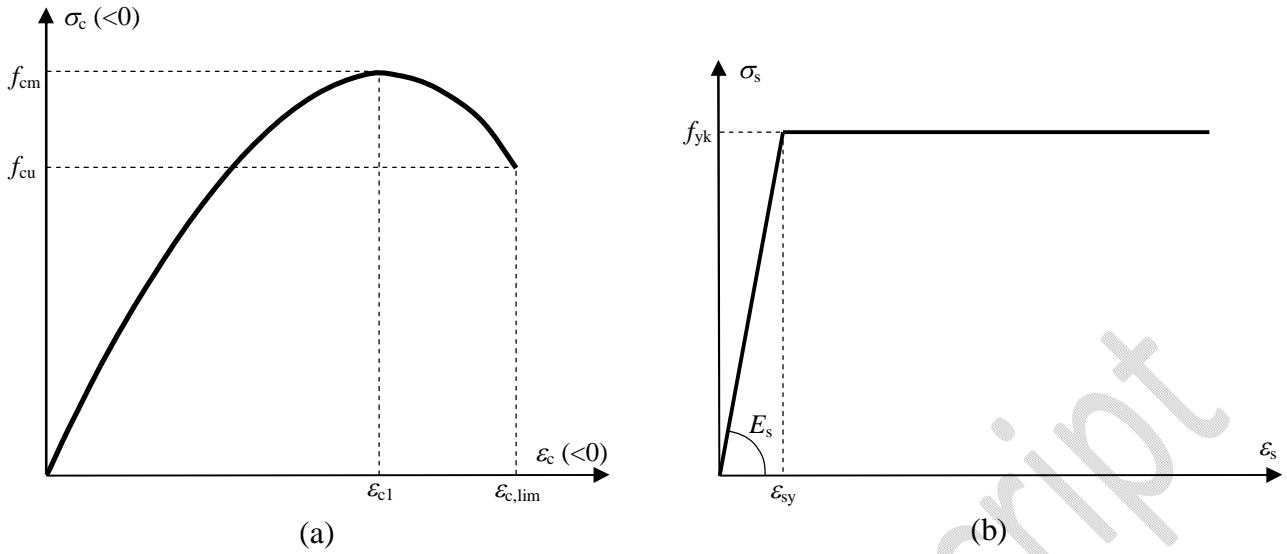
Fig. 2: Stress-strain diagrams for concrete (a) and reinforcing steel (b) adopted in this work.

It is assumed that the yield state of the beam is reached as soon as the stress in the tensile reinforcement σ_s equals the yield strength f_{yk}. The neutral axis depth at the yield state, which is denoted by x_y, can be obtained by imposing translational equilibrium. By referring to Fig. 3, where a doubly reinforced concrete beam is considered, translational equilibrium requires that the following equation be fulfilled at each instant of time:

$$b\int_{0}^{x_y} \sigma_c \, dy + \sigma_{ss} A_{ss} = f_{yk} A_s. \tag{5}$$

Here the subscripts "s" and "ss" are appended to quantities corresponding to tensile and compressive reinforcements, respectively, while the subscript "c" refers to concrete. The meanings of all the geometric quantities relative to the beam cross-section can be inferred from Fig. 3a. By substituting into Eq. (5) the expression of σ_c given by Eq. (4) and by using the linear strain diagram plotted in Fig. 3c, Eq. (5) becomes[‡]

[‡] It is supposed that $\sigma_{ss} < f_{yk}$, as it usually occurs; otherwise, σ_{ss} should be substituted by f_{yk}. The same consideration applies to Eq. (7).

$$ b\,f_{cm}\int_0^{x_y}\left[\frac{k\dfrac{\varepsilon_{sy}}{\varepsilon_{c1}}\dfrac{x_y-y}{d-x_y}-\left(\dfrac{\varepsilon_{sy}}{\varepsilon_{c1}}\dfrac{x_y-y}{d-x_y}\right)^2}{1+(k-2)\dfrac{\varepsilon_{sy}}{\varepsilon_{c1}}\dfrac{x_y-y}{d-x_y}}\right]dy+E_s\,\varepsilon_{sy}\frac{x_y-d'}{d-x_y}A_{ss}=f_{yk}A_s, \tag{6} $$

from which the neutral axis depth at the yield state (x_y) can be calculated. The resistant bending moment of the section at the yield state (M_y) may be determined from the equilibrium of rotation around the tensile reinforcement, which leads to the following formula:

$$ M_y = b\int_0^{x_y}\sigma_c\left(d-y\right)dy+\sigma_{ss}A_{ss}\left(d-d'\right)= $$

$$ = b\,f_{cm}\int_0^{x_y}\left[\frac{k\dfrac{\varepsilon_{sy}}{\varepsilon_{c1}}\dfrac{x_y-y}{d-x_y}-\left(\dfrac{\varepsilon_{sy}}{\varepsilon_{c1}}\dfrac{x_y-y}{d-x_y}\right)^2}{1+(k-2)\dfrac{\varepsilon_{sy}}{\varepsilon_{c1}}\dfrac{x_y-y}{d-x_y}}\right](d-y)\,dy+E_s\,\varepsilon_{sy}\frac{x_y-d'}{d-x_y}A_{ss}\left(d-d'\right). \tag{7} $$
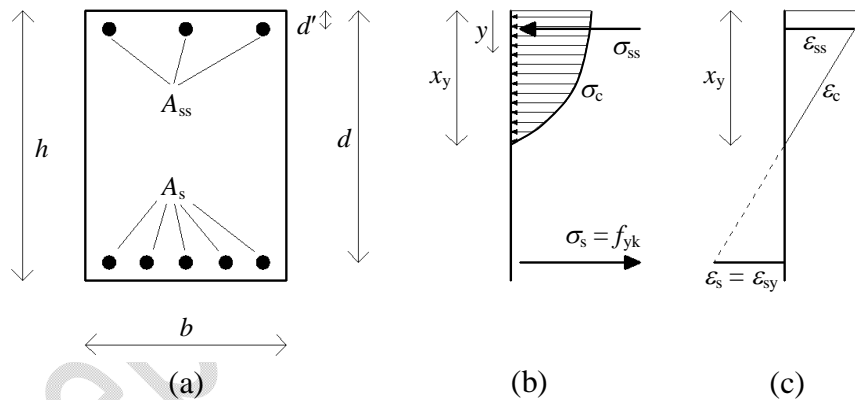

Fig. 3: (a) Sketch of the cross-section of a doubly reinforced concrete beam; (b) stress diagram at the yield state; (c) strain diagram at the yield state.

The ultimate state is reached, instead, when concrete attains its maximum strain $\varepsilon_{c,lim}$. In this case, the stress and strain diagrams over the cross-section are those depicted in Figs. 4a and 4b, respectively. The neutral axis depth at the ultimate state (x_u) can be calculated again from the translational equilibrium condition, which - after using Eq. (4) and the linear strain diagram of Fig. 4b - is given by one of the following two equations:

8

$$b\,f_{cm}\int_0^{x_u}\left[\frac{k\dfrac{\varepsilon_{c,lim}}{\varepsilon_{c1}}\dfrac{x_u-y}{x_u}-\left(\dfrac{\varepsilon_{c,lim}}{\varepsilon_{c1}}\dfrac{x_u-y}{x_u}\right)^2}{1+(k-2)\dfrac{\varepsilon_{c,lim}}{\varepsilon_{c1}}\dfrac{x_u-y}{x_u}}\right]dy+E_s\,\varepsilon_{c,lim}\frac{x_u-d'}{x_u}A_{ss}=f_{yk}A_s \quad \text{if } \sigma_{ss}<f_{yk}\,; \qquad (8a)$$

$$b\,f_{cm}\int_0^{x_u}\left[\frac{k\dfrac{\varepsilon_{c,lim}}{\varepsilon_{c1}}\dfrac{x_u-y}{x_u}-\left(\dfrac{\varepsilon_{c,lim}}{\varepsilon_{c1}}\dfrac{x_u-y}{x_u}\right)^2}{1+(k-2)\dfrac{\varepsilon_{c,lim}}{\varepsilon_{c1}}\dfrac{x_u-y}{x_u}}\right]dy+f_{yk}A_{ss}=f_{yk}A_s \quad \text{if } \sigma_{ss}\geq f_{yk}\,. \qquad (8b)$$

The rotational equilibrium around the tensile reinforcement provides the expression of the resistant

bending moment at the ultimate state (M_u):

$$M_u=b\,f_{cm}\int_0^{x_u}\left[\frac{k\dfrac{\varepsilon_{c,lim}}{\varepsilon_{c1}}\dfrac{x_u-y}{x_u}-\left(\dfrac{\varepsilon_{c,lim}}{\varepsilon_{c1}}\dfrac{x_u-y}{x_u}\right)^2}{1+(k-2)\dfrac{\varepsilon_{c,lim}}{\varepsilon_{c1}}\dfrac{x_u-y}{x_u}}\right](d-y)dy+E_s\,\varepsilon_{c,lim}\frac{x_u-d'}{x_u}A_{ss}(d-d') \quad \text{if } \sigma_{ss}<f_{yk}\,; \;(9a)$$

$$M_u=b\,f_{cm}\int_0^{x_u}\left[\frac{k\dfrac{\varepsilon_{c,lim}}{\varepsilon_{c1}}\dfrac{x_u-y}{x_u}-\left(\dfrac{\varepsilon_{c,lim}}{\varepsilon_{c1}}\dfrac{x_u-y}{x_u}\right)^2}{1+(k-2)\dfrac{\varepsilon_{c,lim}}{\varepsilon_{c1}}\dfrac{x_u-y}{x_u}}\right](d-y)dy+f_{yk}A_{ss}(d-d') \quad \text{if } \sigma_{ss}\geq f_{yk}\,. \qquad (9b)$$
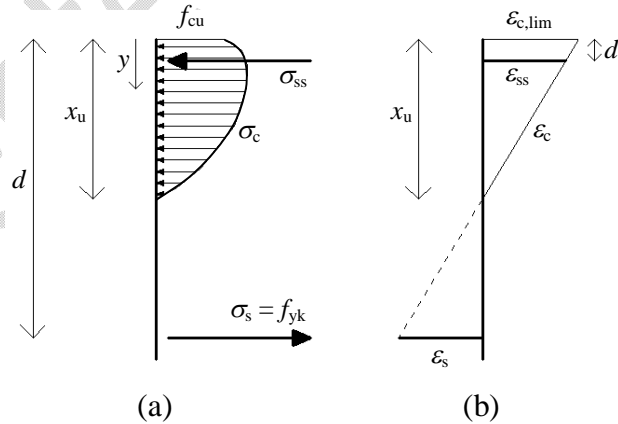

Fig. 4: (a) Stress distribution over the cross-section at the ultimate state; (b) strain diagram at the ultimate

state.

The determination of x_y, M_y, x_u and M_u allows to define the bilinear bending moment - curvature

diagram of the RC beam, which is drawn in Fig. 5a. In this figure, θ_y and θ_u denote the curvatures at the yield and ultimate states, which are given by

$$\theta_y = \frac{\varepsilon_{sy}}{d - x_y} \tag{10}$$

and

$$\theta_u = \frac{\varepsilon_{c,\lim}}{x_u}, \tag{11}$$

respectively.

The parameters $\bar{K}$ and $\bar{M}$ appearing in Eqs. (2) and (3) can be derived from the bilinear diagram of Fig. 5a. More specifically $\bar{K}$, which represents the slope of the diagram plotted in Fig. 5b at $\theta = 0$, can be calculated by this ratio:

$$\bar{K} = \frac{M_y}{\theta_y}. \tag{12}$$

The parameter $\bar{M}$, which represents the equivalent ultimate bending moment, can be obtained by equating the areas A_1 and A_2 under the curves shown in Fig. 5a and 5b, respectively. The equivalence of A_1 and A_2 leads to the following equation:

$$\frac{\bar{M}^2}{\bar{K}} \ln\left[\cosh\left(\frac{\bar{K}}{\bar{M}}\theta_u\right)\right] = \frac{M_u(\theta_u - \theta_y) + M_y\theta_u}{2}, \tag{13}$$

where the left hand term has been obtained by integrating Eq. (2). In this way, the bilinear bending moment - curvature relationship can be substituted by a smoother diagram, which better approximates the real behavior of the beam. In fact, the bending moment – curvature diagram of a real RC beam presents a gradual change of slope when yielding of the tensile reinforcement occurs, as in Fig. 5b, and hence there are no tangent discontinuities, as in Fig. 5a. For this reason, the diagram of Fig. 5b should be preferred to the diagram of Fig. 5a.
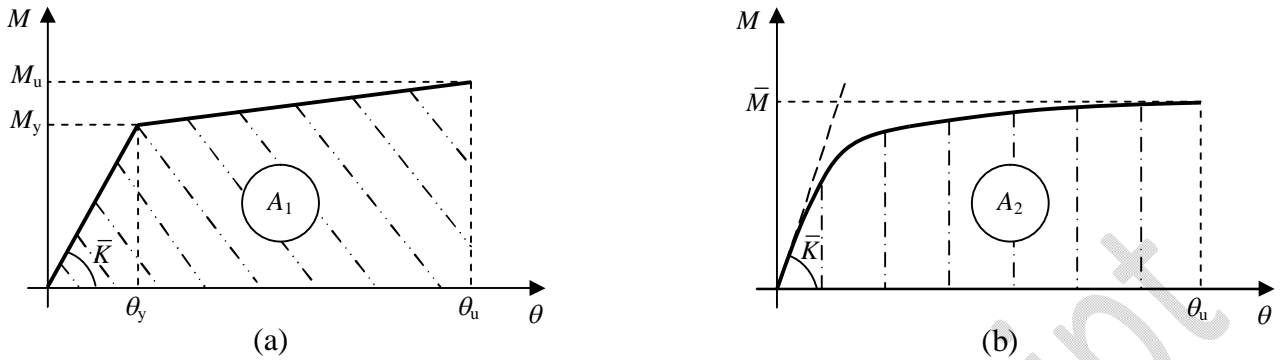
Fig. 5: (a) Bilinear bending moment - curvature relation; (b) smoother bending moment - curvature diagram adopted in this work.

2.3 Strain rate effects for the continuous beam model

The constitutive quantities introduced in Subsection 2.2 are valid only in the static regime. Since dynamic loads are considered in this work and since concrete and steel are strain rate sensitive materials, the static constitutive quantities are updated by using the relations provided by the *CEB Information Bulletin n. 187* [20] (refer also to the recent manuscript by Asprone et al. [21]).

First, the strain rates of concrete and steel reinforcements are easily determined by knowing the rate of curvature and the value of the neutral axis depth. Next, the dynamic properties of concrete and steel reinforcements are evaluated.

For what regards concrete [20,§ 3.3.1], its dynamic strength is given by

$$f_{cm,dyn} = f_{cm} \cdot \left(\frac{\dot{\varepsilon}_c}{30 \cdot 10^{-6}} \right)^{1.026 \cdot \alpha} \quad \text{if } \dot{\varepsilon}_c \leq 30\,\text{s}^{-1}; \tag{14a}$$

$$f_{cm,dyn} = f_{cm} \cdot \gamma \cdot \left(\dot{\varepsilon}_c \right)^{1/3} \quad \text{if } \dot{\varepsilon}_c > 30\,\text{s}^{-1}. \tag{14b}$$

In the formulae above, $\dot{\varepsilon}_c$ is the strain rate of concrete, while $\alpha = 1/(5 + 3 \cdot f_{cm}/4)$ and $\gamma = 10^{\wedge}(6.156 \cdot \alpha - 0.492)$. The concrete strains ε_{c1} and $\varepsilon_{c,lim}$ are augmented by the following expressions (see also [21]):

11

$$\varepsilon_{c1,dyn} = \varepsilon_{c1} \cdot \left(\frac{\dot{\varepsilon}_c}{30 \cdot 10^{-6}}\right)^{0.02} ; \tag{15}$$

$$\varepsilon_{c,lim,dyn} = \varepsilon_{c,lim} \cdot \left(\frac{\dot{\varepsilon}_c}{30 \cdot 10^{-6}}\right)^{0.02} . \tag{16}$$

For what concerns steel [20,§ 3.4.2], its dynamic strength is calculated as

$$f_{yk,dyn} = f_{yk} \cdot \left[1 + \frac{6}{f_{yk}} \ln\left(\frac{\dot{\varepsilon}^s}{5 \cdot 10^{-5}}\right)\right] \quad \text{if } \dot{\varepsilon}^s \leq 10\,\text{s}^{-1} , \tag{17}$$

where $\dot{\varepsilon}^s$ is the strain rate of either tensile or compressive reinforcement. If $\dot{\varepsilon}^s > 10$ s^{-1}, the limit

value 10 s^{-1} is assigned to $\dot{\varepsilon}^s$ in Eq. (17). On the contrary, the module of elasticity E_s is taken as

constant [20,§3.4.3; 21,§2].

It should be pointed out that the dynamic properties of concrete and steel are updated at each time

step of the calculation, as detailed in the next subsection.

2.4 Iterative procedure for the integration of the equation of motion

First, the static mechanical characteristics (i.e. the neutral axis depth and the bending moment at

yield and ultimate states), which are determined from Eqs. (6)-(9), are used to calculate the

parameters $\bar{K}$ and $\bar{M}$ through Eqs. (12) and (13). Then, the initial conditions are imposed and the

space and time steps are specified.

Next, an iterative procedure is performed, which consists in evaluating at each time step the

following quantities:

1) the vertical displacement v, which is obtained by solving Eq. (3) (for instance, by employing

either an explicit or an implicit version of the Finite Difference Method, after setting the proper

initial and boundary conditions), where $\bar{K}$ and $\bar{M}$ are varied at each time step due to strain rate

effects;

2) the curvature $\theta = -\partial^2 v/\partial x^2$ and the rate of curvature $\dot{\theta} = \partial\theta/\partial t$;

3) the bending moment M corresponding to the curvature θ from Eq. (2);

4) the neutral axis depth from rotational equilibrium around the tensile reinforcement under the

applied bending moment M;

5) the strains of concrete and steel reinforcements by using the linear deformation diagram and the value of curvature;

6) the strain rates of concrete and steel reinforcements;

7) the updated dynamic properties of materials by means of Eqs. (14)-(17);

8) the updated values of the mechanical characteristics (x_y, M_y, x_u, M_u), by which the values of $\bar{K}$ and $\bar{M}$ are modified.

The loop is ended when the collapse criterion, which has been defined as the attainment of the maximum concrete strain (ultimate state), is satisfied.

3. SDOF model

In this section it is discussed how to assess the dynamic response of the beam by means of a single degree of freedom (SDOF) model. In Fig. 6a a real beam is depicted (which, as an example, is supposed to be simply supported and subjected to a uniformly distributed load, as that examined in Section 4), while its equivalent SDOF system is sketched in Fig. 6b. It should be noted that damping is disregarded, since successive cycles of loading are not considered; in fact, the first peak displacement is the more severe condition, because it is unlikely that the structure collapses after unloading [18].
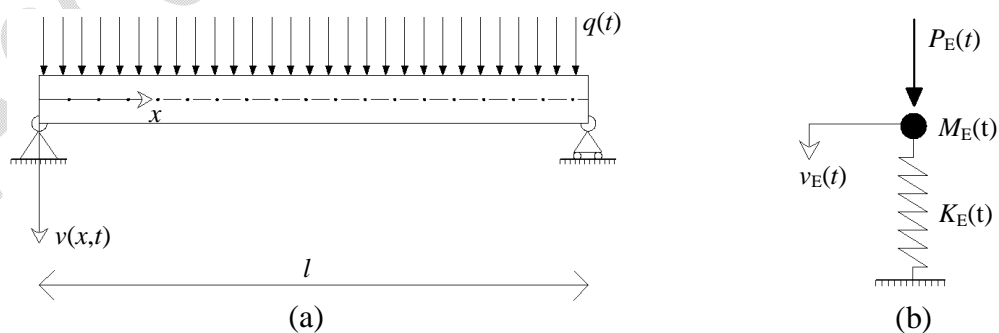

Fig. 6: (a) Real beam; (b) equivalent SDOF model of the real beam.

3.1 Load-displacement diagram of the SDOF system

The elastic-plastic behavior of the SDOF system can be represented by a bilinear load-displacement diagram, as shown in Fig. 7b. The latter can be derived from the bending moment - curvature diagram of the beam (plotted first in Fig. 5a and re-drawn in Fig. 7a), as described in the following.
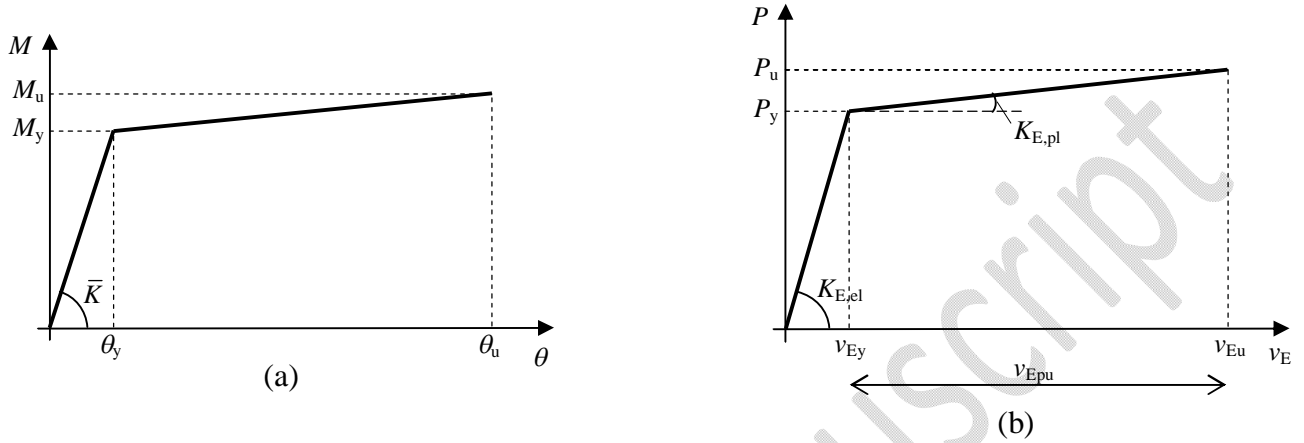

Fig. 7: (a) Bilinear bending moment - curvature diagram of the beam; (b) corresponding bilinear load - displacement diagram of the equivalent SDOF model.

The yield load P_y is easily determined from the yield bending moment M_y by means of equilibrium considerations:

$$M_y = \frac{q_y \cdot l^2}{8} \quad \Rightarrow \quad P_y = q_y \cdot l = \frac{8 \cdot M_y}{l}, \tag{18}$$

where q_y is the uniformly distributed load acting on the beam at the yield state. The yield displacement v_{Ey} can be calculated from the well-known formula provided by the linear elastic theory of beams:

$$v_{Ey} = \frac{5 \cdot q_y \cdot l^4}{384 \cdot \bar{K}} = \frac{5 \cdot P_y \cdot l^3}{384 \cdot \bar{K}}, \tag{19}$$

where $\bar{K} = M_y / \theta_y$ is the elastic bending rigidity of the beam (see Fig. 7a). Hence, the elastic stiffness of the SDOF system is given by

$$K_{E,el} = \frac{P_y}{v_{Ey}} = \frac{384 \cdot \bar{K}}{5 \cdot l^3}. \tag{20}$$

The ultimate load P_u can again be obtained from equilibrium conditions:

$$M_u = \frac{q_u \cdot l^2}{8} \quad \Rightarrow \quad P_u = q_u \cdot l = \frac{8 \cdot M_u}{l}, \tag{21}$$

where q_u is the uniformly distributed load on the beam at the ultimate state. The ultimate

displacement v_{Eu} is evaluated by assuming that a concentrated plastic hinge is formed at the mid-

span section of the beam, as shown in Fig. 8a. Here φ_p indicates the plastic rotation at any time after

the generation of the plastic hinge, while v_{Ep} represents the corresponding plastic displacement at

the mid-span section. At the ultimate state $\varphi_p = \varphi_{pu}$, hence the total plastic displacement $v_{Ep} = v_{Epu}$

can be calculated as

$$v_{Epu} = \frac{\varphi_{pu}}{2} \cdot \frac{l}{2}. \tag{22}$$

By introducing the plastic hinge length l_p (see Fig. 8b) and by denoting the total plastic curvature by

θ_p ($\theta_p = \theta_u - \theta_y$), which is assumed to be constant over l_p, the ultimate displacement v_{Eu} can be

finally derived:

$$v_{Eu} = v_{Ey} + v_{Epu} = v_{Ey} + \frac{\varphi_{pu}}{2} \cdot \frac{l}{2} = v_{Ey} + \frac{\theta_p \cdot l_p}{2} \cdot \frac{l}{2} = v_{Ey} + \frac{1}{4} \cdot (\theta_u - \theta_y) \cdot l_p \cdot l. \tag{23}$$

Finally, the plastic stiffness of the SDOF system is given by

$$K_{E,pl} = \frac{P_u - P_y}{v_{Eu} - v_{Ey}}. \tag{24}$$

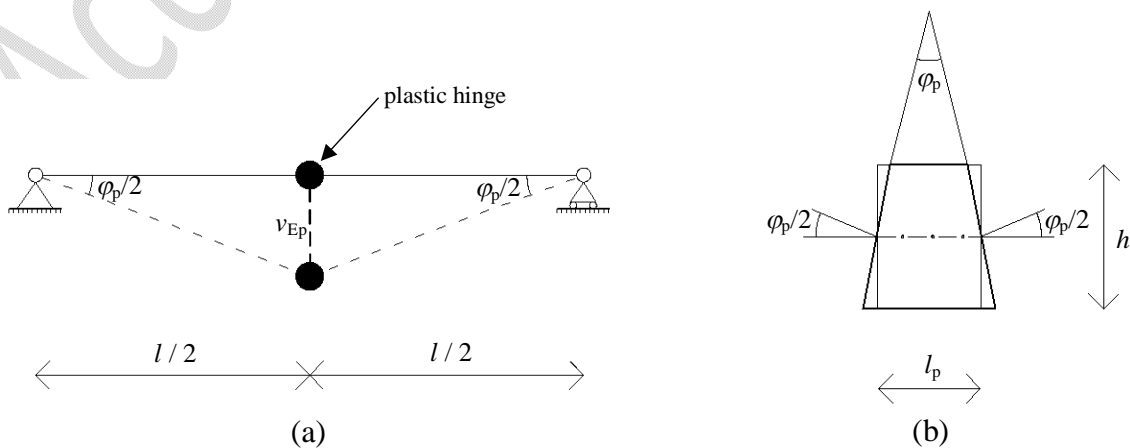(a)   (b)

Fig. 8: (a) Plastic deflections of the beam with a concentrated plastic hinge at the mid-span section; (b)

15

schematic representation of the plastic hinge.

The main drawback of this approach is that the plastic hinge length l_p cannot be determined *a priori*.

Many approximate expressions for l_p are available in literature. Here, the simple formula provided

by Mattock (see [7]) is adopted:

$$l_p = d + 0.05 \cdot l. \tag{25}$$

3.2 Equations of motion of the SDOF system

The motion of the SDOF system under an external dynamic force P_E is described by the following

set of ordinary differential equations (refer to Figs. 6b and 7b):

$$M_{E,el} \frac{d^2 v_E(t)}{dt^2} + K_{E,el}(t) v_E(t) = P_E(t) \quad \text{for } 0 \le v_E \le v_{Ey}; \tag{26a}$$

$$M_{E,pl} \frac{d^2 v_E(t)}{dt^2} + K_{E,pl}(t) v_E(t) + \left(K_{E,el}(t) - K_{E,pl}(t)\right) v_{Ey} = P_E(t) \quad \text{for } v_{Ey} < v_E \le v_{Eu}. \tag{26b}$$

It is important to observe that the elastic and plastic stiffnesses ($K_{E,el}$ and $K_{E,pl}$) depend on time t,

since they are updated at each step of the calculation due to strain rate effects, as explained in

Subsection 3.3.

The equivalent load P_E is simply given by $P_E = q \cdot l$. The elastic and plastic equivalent masses ($M_{E,el}$

and $M_{E,pl}$) are obtained by multiplying the total mass of the beam (M_b) by a "load-mass factor",

which depends both on the type of regime (either elastic or plastic) and on the beam supports and

loads; in particular, for a simply supported beam with a uniformly distributed load, $M_{E,el} = 0.78 \cdot M_b$

and $M_{E,pl} = 0.66 \cdot M_b$ [12,Table 5.1].

3.3 Strain rate effects for the SDOF system

The effects of strain rate are taken into account for the equivalent SDOF model too. Since the

dynamic properties of the materials are given in terms of their strain rates (see Eqs. (14)-(17)), it is

necessary to relate the SDOF system to the associated (real) beam, by which the strain rates of

concrete and steel can be assessed.

Once the equivalent displacement v_E and equivalent velocity $\dot{v}_E = dv_E / dt$ are calculated at each

time step by solving either Eq. (26a) or Eq. (26b), the curvature θ_E and the curvature rate

$\dot{\theta}_E = d\theta_E / dt$ at the mid-span section of the associated beam can be evaluated. In the elastic regime,

θ_E and $\dot{\theta}_E$ are obtained from linear elastic theory; in particular, for a simply supported beam with a

uniformly distributed load, they are given by:

$$\theta_E = \frac{48 \cdot v_E}{5 \cdot l^2} \quad \text{for } 0 \leq v_E \leq v_{Ey} ; \tag{27a}$$

$$\dot{\theta}_E = \frac{48 \cdot \dot{v}_E}{5 \cdot l^2} \quad \text{for } 0 \leq v_E \leq v_{Ey} . \tag{27b}$$

In the plastic regime, instead, it is supposed that a concentrated plastic hinge is generated at the

mid-span section of the associated beam, as shown in Fig. 8a. Accordingly, in this case θ_E and $\dot{\theta}_E$

can be evaluated through the following expressions:

$$\theta_E = \theta_y + \frac{\varphi_p}{l_p} = \theta_y + 2 \cdot \frac{v_{Ep}}{l/2} \cdot \frac{1}{l_p} = \theta_y + 2 \cdot \frac{v_E - v_{Ey}}{l/2} \cdot \frac{1}{l_p} \quad \text{for } v_{Ey} \leq v_E \leq v_{Eu} ; \tag{28a}$$

$$\dot{\theta}_E = 2 \cdot \frac{\dot{v}_E}{l/2} \cdot \frac{1}{l_p} \quad \text{for } v_{Ey} \leq v_E \leq v_{Eu} . \tag{28b}$$

At each step of the calculation, the value of θ_E (given by either Eq. (27a) or Eq. (28a)) allows to

determine the value of the bending moment M from the bending moment - curvature diagram of

Fig. 7a. Then, by imposing rotational equilibrium about the tensile reinforcement, the neutral axis

depth (here denoted as $\bar{x}$) can be easily evaluated. Finally, the strain rates of concrete and of tensile

and compressive steel reinforcements are calculated through the following formulae:

$$\dot{\varepsilon}_c = \dot{\theta}_E \cdot \bar{x} ; \tag{29a}$$

$$\dot{\varepsilon}_s = \dot{\theta}_E \cdot (d - \bar{x}); \tag{29b}$$

$$\dot{\varepsilon}_{ss} = \dot{\theta}_E \cdot (\bar{x} - d'). \tag{29c}$$

The absolute values of the strain rates given by Eqs. (29) are introduced into Eqs. (14)-(17) to

update the properties of the materials.

It is apparent that the procedure described above contains some approximations. This is one of the

reasons why the continuous beam model discussed in Section 2 should be preferred to the simpler

SDOF model presented here.

4. Application

In this section, the theoretical models described in Sections 2 and 3 are applied to a practical

example. In particular, a simply supported beam subjected to a uniformly distributed load generated

by an explosion is considered.

The theoretical results are compared with some experimental findings obtained by Magnusson and

Hallgren [2], who tested several simply supported RC beams under shock waves produced by air

blast. As the same authors point out in their paper, the explosive charge was located far enough

from the beam to generate a plane wavefront, hence a uniformly distributed load. All the details

regarding the beams examined in this work are reported in Appendix A.

First, the beam labeled by B40-D5 is examined. The parameter chosen to compare the experimental

data with the theoretical results is the deflection at the mid-span section of the beam, which

obviously represents the maximum deflection and which is henceforth indicated by v_{max}. The

experimental time-history of v_{max} relative to beam B40-D5 is plotted in solid black line in Fig. 9.

The latter has been cut off when the maximum experimental concrete strain is reached, in

accordance with the assumption made in this paper that failure occurs when concrete attains its

maximum strain.

The dashed black line of Fig. 9 represents instead the time-history of v_{max} obtained by integrating

Eq. (3), which is derived from the continuous beam model proposed in this work. This partial

differential equation is solved by means of the Finite Difference Method. Since the beam is at rest

before the shock wave impinges on it, null initial conditions are imposed (which means that the

displacements and velocities along the beam at the beginning of the calculation are taken equal to

zero), while the boundary conditions state that the vertical displacement and the curvature must

vanish at the ends of the beam. All the derivatives (both in space and time) are computed with a 2nd order approximation. At each time step, the displacements in the beam are calculated explicitly[§] by using the values at previous time steps. Convergence of results is reached by taking a time step of 10^{-6} s and a space step of 0.05 m; in fact, the results produced by the Finite Difference code after decreasing the time and space steps do not show a significant variation. The maximum strains in the materials given by the continuous beam model are $\varepsilon_{c,lim,dyn} = 0.0044$, $\varepsilon_s = 0.0056$ and $\varepsilon_{ss} = 0.002$. Yielding is reached only in the tensile reinforcement.

The time-history of the maximum deflection predicted by the SDOF model is shown in dotted black line in Fig. 9. This curve is determined from the ordinary differential equations (26), which are integrated in time by employing again the explicit version of the Finite Difference Method and by imposing zero initial conditions (i.e. v_E ($t=0$) = dv_E/dt ($t=0$) = 0). The chosen time step is identical to that adopted for the continuous beam model.

Finally, the grey curve of Fig. 9 corresponds to the finite element (FE) solution given by the commercial software *Midas Gen 2012 (v2.1)*. In particular, the fiber model of this software is used, which consists in dividing the cross-section of the beam into concrete fibers and steel rebars. For what concerns the material models, a trilinear relationship between stress and strain is used for concrete, which approximates with high precision the compressive stress-strain diagram shown in Fig. 2a (the tensile strength of concrete is instead neglected, in agreement with the assumptions made in this work); for steel rebars, an elastic – perfectly plastic stress-strain diagram is adopted, as that shown in Fig. 2b. The variation of the compressive zone depth during time is computed by the Finite Element software, which thus handles the transition from compression to tension across the cross-section automatically. In order to take into consideration the effects of strain rate, which are not accounted for by *Midas Gen 2012 (v2.1)*, the dynamic properties of the material given by the continuous beam model at the last step of the calculation (which correspond to the ultimate strain

---

[§] It should be noted that also an implicit version of the Finite Difference Method has been used, which requires a higher computational effort though providing the same results.

rates reached in the analysis of the continuous beam model) are introduced as constants into the FE model. If the static properties of the materials were used instead, the FE software would have provided an even lower ultimate deflection. The meshes in space and time used in the FE software are identical to those adopted for the continuous beam model. Lastly, it should be underlined that, since the software does not include a failure criterion for concrete crushing, the time-history provided by the FE solution is interrupted at the instant of time when the maximum concrete strain obtained from the continuous beam model (that is $\varepsilon_{c,lim,dyn} = 0.0044$) is reached.
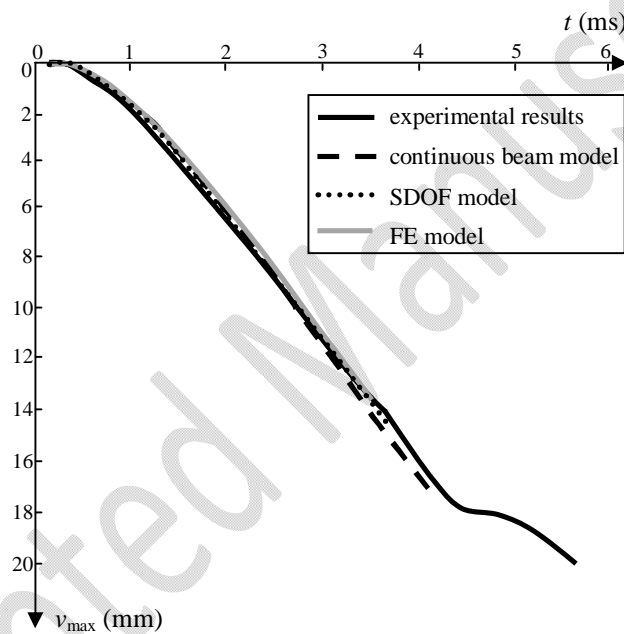
Fig. 9: Time-histories of the maximum deflection of beam B40-D5 (tested in [2]) calculated by means of different theoretical models, and comparison with experimental findings.

The experimental time-history of the maximum deflection of another beam analyzed by Magnusson and Hallgren [2], labeled by B200/40-D3, is reported in Fig. 10, together with its theoretical predictions given by the continuous beam model, the SDOF model and the FE model. For this beam, the maximum concrete strain produced by the continuous beam model, which is used to truncate the deflection time-history derived from the FE model, is $\varepsilon_{c,lim,dyn} = 0.005$. Whilst, the maximum steel strains calculated from the continuous beam model are $\varepsilon_s = 0.028$ and $\varepsilon_{ss} = 0.0026$;

20

also in this case, yielding is reached in the tensile reinforcement only.

The maximum experimental concrete strains of both beams are reported for comparison in Table A.1.
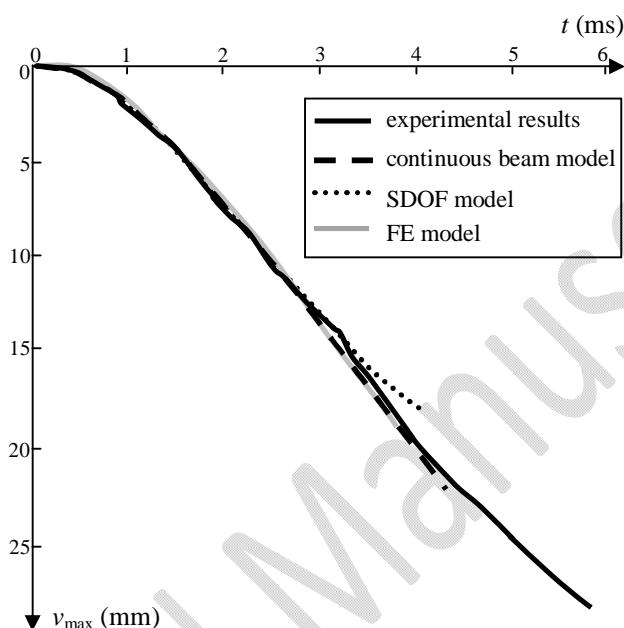

Fig. 10: Comparison between the experimental outcomes (provided in [2]) and the theoretical results provided by different approaches relative to beam B200/40-D3.

Figs. 9 and 10 show that the continuous beam model presented in this work is the one that best agrees with experimental data.[**] In particular, the continuous beam model gives the most accurate assessment of the maximum deflection of the beam at failure. On the other hand, the FE solution always underestimates the maximum displacement of the beam at collapse, while the prediction of the SDOF model sometimes diverges from the experimental curve (see Fig. 10).

Besides being capable of fitting well the actual time-history of the maximum deflection of the beam, the continuous beam model can also provide other useful information, such as the displacement and curvature profiles along the beam axis at a certain instant of time, which instead

---

[**] This statement is confirmed by the investigation of other beams tested in [2], the outcomes of which are not reported here for the sake of brevity.

cannot be determined from the SDOF model. For instance, Figs. 11a and 11b show, respectively, the diagrams of the beam vertical displacements and curvatures at different instants of time relative to beam B40-D5. It can be observed from the figures that the vertical displacement and curvature profiles at the first instants of time (e.g. at $t = 1$ ms) exhibit changes in concavity along the length of the beam, due to inertia effects. As the time passes by, the deflection and curvature profiles assume the typical shapes they show in the static case. This interesting consideration could not have been drawn from the SDOF model, which can provide the values of deflection and curvature only at the mid-span section of the beam.
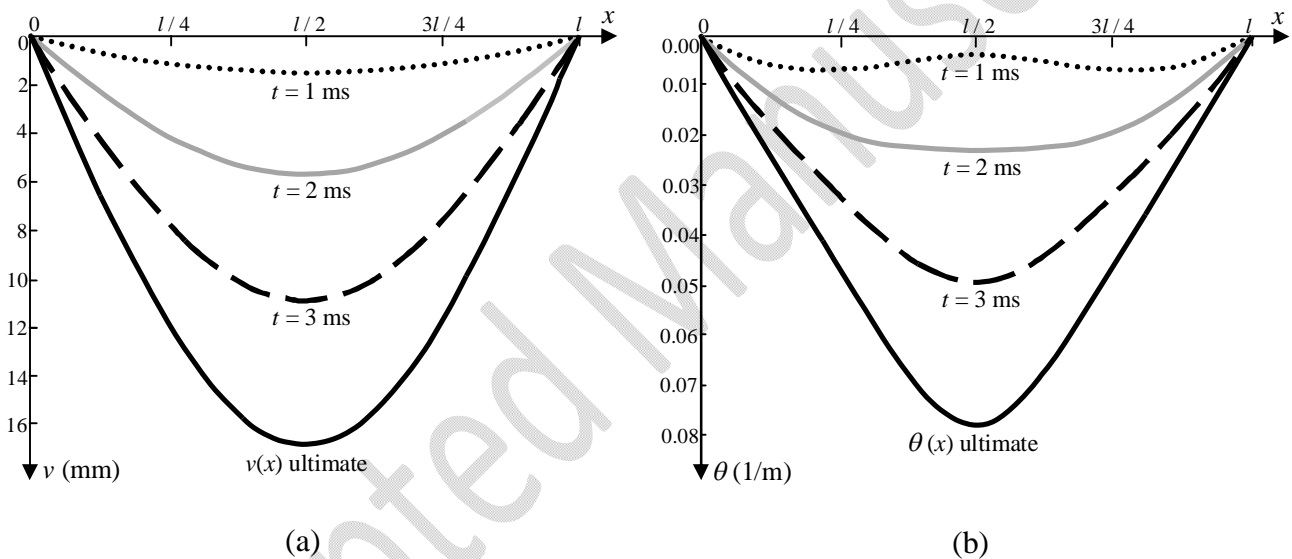

(a)   (b)

Fig. 11: Vertical displacements (a) and curvatures (b) of beam B40-D5 at different times predicted by the continuous beam model.

5. Conclusions

In this work, a continuous model which aims at predicting the behavior of reinforced concrete beams under blast loads has been described. The corresponding equation of motion, which is based on a smooth nonlinear relation between bending moment and curvature, is rather straightforward and easy to integrate (for example through the Finite Difference Method); nonetheless, it gives an accurate estimate of the time-history of the beam maximum displacement and, in particular, of its

value at failure, as shown by comparison with experimental data. The efficacy of the model derives also from having included into the formulation the effects of strain rate on the properties of the materials.

An alternative approach has also been presented, which consists in idealizing the beam as an equivalent SDOF system, as is common in practical applications. This approach, in which strain rate effects are again accounted for, is more convenient than the continuous beam model from a computational point of view, but it presents two main drawbacks: the first is that it requires the use of approximate formulae to define some quantities (such as, for instance, the coefficients which convert the total mass of the beam into the SDOF mass and the length of the plastic hinge); the second is that it cannot provide some useful information, like the profiles of displacement, rotation and curvature along the beam at any instant of time. Furthermore, it is less accurate than the continuous beam model.

In concluding the paper, the two major limitations of the proposed continuous beam model should be emphasized: first, shear deformation and rotary inertia have been neglected, since Euler-Bernoulli's theory has been adopted; second, displacements and rotations have been assumed to be small. Thus, future research will focus on overcoming these limitations by employing Timoshenko's theory and by considering large deformations, respectively. Furthermore, a different failure criterion could be defined: since the maximum displacement predicted by the proposed approach underestimates the actual value found experimentally, the calculation of the maximum deflection could be carried on after the first concrete fiber reaches its maximum strain (which represents the collapse criterion considered here); then, in order to account for the portion of crushed concrete, the depth of the cross-section could be decreased until equilibrium ceases to exist. Finally, future work will also check the validity of the continuous beam model when the beam is subjected to other dynamic loads, like concentrated forces produced by the impact of falling objects.

Appendix A

This appendix contains detailed information about the material properties and the loads relative to

the two beams - tested by Magnusson and Hallgren - analyzed in this paper, which are denoted as

B40-D5 and B200/40-D3 in [2].

A sketch of the experimental apparatus set up by Magnusson and Hallgren is shown in Fig. A.1. All

the beams were simply supported, had a span of 1.5 m and a rectangular cross-section, and were

reinforced with both tensile and compressive bars and with stirrups. The other geometric and
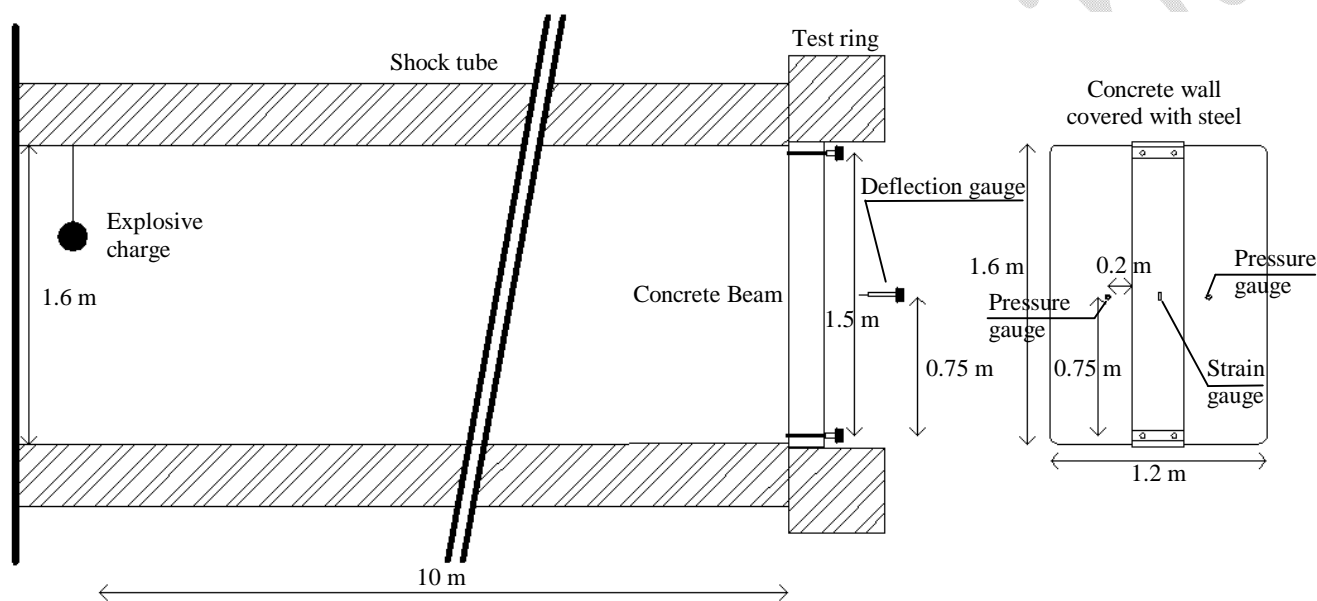
mechanical characteristics of the beams are summarized in Table A.1.

Fig. A.1: Experimental apparatus used by Magnusson and Hallgren [2].

	B40-D5	B200/40-D3
width of the cross-section	0.300 m	0.293 m
depth of the cross-section	0.160 m	0.160 m
cover	0.025 m	0.025 m
tensile reinforcement	5 ϕ16 mm	5 ϕ16 mm
compressive reinforcement	2 ϕ10 mm	2 ϕ10 mm
concrete compressive strength [a]	43 MPa	173/54 MPa [b]
registered maximum concrete strain	3.69 ‰	5.03 ‰
steel yield strength	604 MPa	555 MPa

steel elastic modulus	210 GPa	204 GPa
mass per unit length	--- [c]	130 kg/m

[a] It refers to the compressive strength of ϕ150x300 mm concrete cylinders.
[b] The beam was made of two concrete layers: the first value refers to the concrete in the compressive zone, while the second is relative to the concrete in the tensile zone.
[c] This value has not been provided by the authors, so it has been assumed equal to 120 kg/m = 2500 kg/m^3 x 0.3 m x 0.16 m.

Table A.1: Properties of the beams studied in this work (extrapolated from [2]).

The two beams were subjected to the pressures shown in Figs. A.2 and A.3. Each figure presents two diagrams, since two pressure gauges were used by Magnusson and Hallgren to register the pressure generated by the explosive charge on each beam. The results of Section 4 have been obtained by applying, on each beam, the average pressure between the two curves. The diagrams of Figs. A.2 and A.3 have been interrupted at $t = 6$ ms, since for both beams the maximum deflection at failure occurs at a time $t < 6$ ms (see Figs. 9 and 10). It is important to remark that, after concrete crushing, both beams continued to move due to inertia effect, dissipating the amount of energy acquired from the blast load. The experimental gauges recorded these further displacements, but for our structural analysis they are meaningless since concrete is already crushed at this stage.
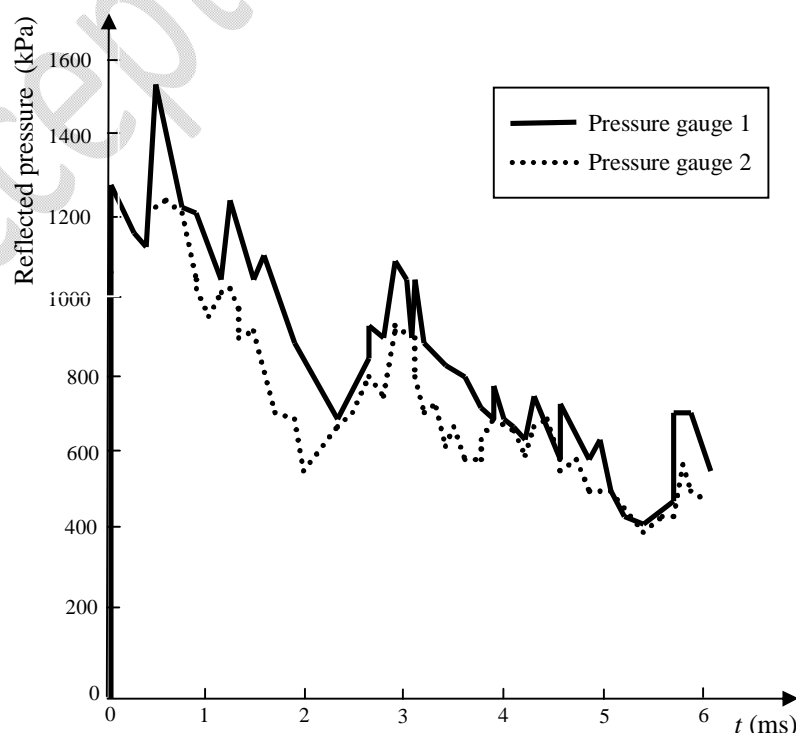
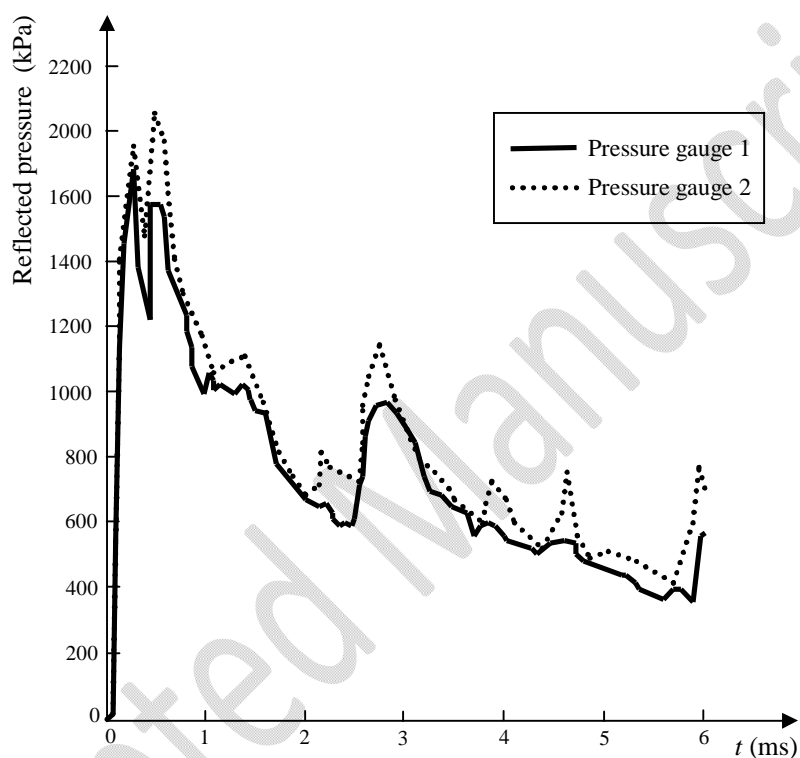**Fig. A.2:** Recorded pressure for beam B40-D5 (derived from [2,Fig. A1.6]).

Fig. A.3: Recorded pressure for beam B200/40-D3 (derived from [2,Fig. A1.26]).

Acknowledgements

References

[1] Hudson JL, Darwin D. Evaluation and repair of blast damaged reinforced concrete buildings. SL Report 05-1, University of Kansas Center for Research, Inc., Lawrence, Kansas, USA; 2005.

[2] Magnusson J, Hallgren M. High performance concrete beams subjected to shock waves from air blast. Report n. FOA-R--00-01586-311--SE, Defence Research Establishment (FOA), Tumba, Sweden; 2000.

[3] Magnusson J, Hallgren M. High performance concrete beams subjected to shock waves from air blast, Part 2. Report n. FOI-R--1116--SE, Swedish Defence Research Agency (FOI), Tumba, Sweden; 2003.

[4] Magnusson J, Hallgren M. Reinforced high strength concrete beams subjected to air blast loading. In: Jones N, Brebbia CA, editors. Structures under shock and impact VIII. Southampton : WIT Press; 2004, p. 53-62.

[5] Magnusson J, Hallgren M, Ansell A. Air-blast-loaded, high-strength concrete beams. Part I: Experimental investigation. Mag Concr Res 2010; 62: 127-36.

[6] Remennikov AM, Kaewunruen S. Impact resistance of reinforced concrete columns: experimental studies and design considerations. Proceedings of the 19th Australasian Conference on the Mechanics of Structures and Materials; 2006 Nov 29 - Dec 1; Christchurch, New Zealand. Tailor & Francis; 2007, p. 817-24.

[7] Fujikake K, Li B, Soeun S. Impact response of reinforced concrete beam and its analytical evaluation. J Struct Eng ASCE 2009; 135: 938-50.

[8] Tachibana S, Masuya H, Nakamura S. Performance based design of reinforced concrete beams under impact. Nat Hazards Earth Syst Sci 2010; 10: 1069-78.

[9] Alves M, Jones N. Impact failure of beams using damage mechanics: Part II – Application. Int J Impact Eng 2002; 27: 863-90.

[10] Lawver D, Daddazio R, Vaughan D, Stanley M, Levine H. Response of AISC steel column sections to blast loading. Proceedings of the ASME 2003 Pressure Vessels and Piping Conference;

2003 Jul 20-24; Cleveland, Ohio, USA. New York: ASME; 2003, p. 139-48.

[11] Nassr AA, Razaqpur AG, Tait MJ, Campidelli M, Foo S. Single and multi degree of freedom analysis of steel beams under blast loading. Nucl Eng Des 2012; 242: 63-77.

[12] Biggs JM. Introduction to structural dynamics. New York: McGraw-Hill Book Company; 1964.

[13] Magnusson J. Structural concrete elements subjected to air blast loading [Licentiate thesis]. TRITA-BKN Bulletin 92. Stockholm (Sweden): Royal Institute of Technology; 2007.

[14] Yang G, Lok T-S. Analysis of RC structures subjected to air-blast loading accounting for strain rate effect of steel reinforcement. Int J Impact Eng 2007; 34: 1924-35.

[15] Fischer K, Häring I. SDOF response model parameters from dynamic blast loading experiments. Eng Struct 2009; 31: 1677-86.

[16] Magnusson J, Ansell A, Hansson H. Air-blast-loaded, high-strength concrete beams. Part II: Numerical non-linear analysis. Mag Concr Res 2010; 62: 235-42.

[17] Graff KF. Wave motion in elastic solids. New York: Dover Publications, Inc.; 1991.

[18] Riedel W, Fischer K, Kranzer C, Erskine J, Cleave R, Hadden D et al. Modeling and validation of wall-window retrofit system under blast loading. Eng Struct 2012; 37: 235-45.

[19] Federal Institute of Technology. Model Code 2010, First Complete Draft, Volume 1. Lausanne (Switzerland): fib Bulletin 55; 2010.

[20] Comité Euro-International du Béton. Concrete structures under impact and impulsive loading. Lausanne (Switzerland): CEB Bulletin 187; 1988.

[21] Asprone D, Frascadore R, Di Ludovico M, Prota A, Manfredi G. Influence of strain rate on the seismic response of RC structures. Eng Struct 2012; 35: 29-36.

List of figures captions

Fig. 1: Internal and external forces acting on an infinitesimal element of the beam.

Fig. 2: Stress-strain diagrams for concrete (a) and reinforcing steel (b) adopted in this work.

Fig. 3: (a) Sketch of the cross-section of a doubly reinforced concrete beam; (b) stress diagram at the yield state; (c) strain diagram at the yield state.

Fig. 4: (a) Stress distribution over the cross-section at the ultimate state; (b) strain diagram at the ultimate state.

Fig. 5: (a) Bilinear bending moment - curvature relation; (b) smoother bending moment - curvature diagram adopted in this work.

Fig. 6: (a) Real beam; (b) equivalent SDOF model of the real beam.

Fig. 7: (a) Bilinear bending moment - curvature diagram of the beam; (b) corresponding bilinear load - displacement diagram of the equivalent SDOF model.

Fig. 8: (a) Plastic deflections of the beam with a concentrated plastic hinge at the mid-span section; (b) schematic representation of the plastic hinge.

Fig. 9: Time-histories of the maximum deflection of beam B40-D5 (tested in [2]) calculated by means of different theoretical models, and comparison with experimental findings.

Fig. 10: Comparison between the experimental outcomes (provided in [2]) and the theoretical results provided by different approaches relative to beam B200/40-D3.

Fig. 11: Vertical displacements (a) and curvatures (b) of beam B40-D5 at different times predicted by the continuous beam model.

Fig. A.1: Experimental apparatus used by Magnusson and Hallgren [2].

Fig. A.2: Recorded pressure for beam B40-D5 (derived from [2,Fig. A1.6]).

Fig. A.3: Recorded pressure for beam B200/40-D3 (derived from [2,Fig. A1.26]).

List of tables captions

Table A.1: Properties of the beams studied in this work (extrapolated from [2]).